Experimental characterization and yield strength model for process-structure-property of selective laser melted 316L

Yefeng Chen[a,b], Xiaowei Wang[a,b,], Dong Li[a,b], Dewen Zhou[a,b], Yong Jiang[a,b], Xinyu Yang[d,e], Chenglu Liu[c], Sean B.Leen[e], Jianming Gong[a,b,*]*

[a] *School of Mechanical and Power Engineering, Nanjing Tech University, Nanjing 211816, PR China;*

[b] *Jiangsu Key Lab of Design and Manufacture of Extreme Pressure Equipment, Nanjing 211816, PR China;*

[c] *Key Laboratory for Light-Weight Materials, Nanjing Tech University, Nanjing 211816, PR China;*

[d] *Institute of High Performance Computing, A*STAR Research Entities, 1 Fusionopolis Way, #16-16 Connexis, 138632, Singapore*

[e]*Mechanical Engineering, School of Engineering, College of Science and Engineering, NUI Galway, Ireland*

***Corresponding authors:**

E-mail: *xwwang@njtech.edu.cn (Xiaowei Wang); gongjm@njtech.edu.cn (Jianming Gong)*

Abstract

Heat treatment is the most common method to relieve residual stress and to adjust tensile properties in additively manufactured material. However, the well-known strengthening factors (e.g., dislocation density, cellular sub-structure, low angle grain boundaries, nano-oxide particle) in selective laser melted 316L (SLM 316L) are strongly influenced by heat-treatment temperature. In this work, horizontal and vertical oriented SLM 316L specimens are heat treated from 550 ℃ to 1150 ℃, followed by tensile tests and microstructural characterization. With increasing temperature, strength (e.g., yield strength, ultimate tensile strength) is found to decrease and elongation is found to increase. The heat treatments of 550 ℃, 650 ℃ and 750 ℃ lead to coarsening of cellular sub-structure. Furthermore, the cellular sub-structure and melt boundaries annihilate at 950 ℃. When the temperature reaches 1150 ℃, SLM 316L has finished recrystallization with volume fraction of nano-oxide particles increasing greatly. Based on microstructural characterization, the proposed model, considering strengthening mechanisms of cellular sub-structure, nano-oxide particle and grain boundaries, give satisfactory accuracy to predict yield strength for horizontal orientation. The yield strength for vertical orientation can also be predicted by this model when modified by consideration of anisotropy of columnar grains and lack-of-fusion defects. The anisotropy and lack-of-fusion lead

to 5.4% reduction in yield strength for the vertical orientation. This work establishes quantitative relationships for heat treatment-microstructure-property, in which the anisotropy of tensile properties is considered.

Keywords: Selective laser melting; 316L; Heat treatment; Tensile property; Microstructure

1. Introduction

Selective laser melting (SLM) technology, as one of a number of different additive manufacturing (AM) techniques, fabricates complex components using powder via layer by layer laser scanning [1, 2]. Among the various metal AM techniques, SLM is often employed due to its noticeable advantages of low porosity and high accuracy [3]. As research has progressed, many metals, such as steel, titanium, aluminum and nickel have been adopted in SLM technology [4]. 316L austenitic stainless steel, which has outstanding corrosion resistance [5], excellent oxidation resistance and good formability [6], is widely used with SLM due to its high laser absorption [7] and high ductility. In the as-built condition, SLM 316L has improved mechanical properties and a distinct microstructure compared with traditional 316L. As is well known, the mechanical properties are directly influenced by microstructure. Microstructure, in turn, is directly influenced by post heat treatment which is a standard step before engineering application[8]. The establishment of the quantitative relationship between heat treatment, microstructure and mechanical properties in SLM 316L is essential for engineering application.

Since Abe et al. [9] tried to fabricate 316L parts by SLM significant research has been conducted on the mechanical properties of SLM 316L. SLM 316L exhibits a high yield strength, of almost twice that of traditional 316L [10]. This is mainly attributed to a high density of dislocations and a cellular sub-structure [11] due to the very high cooling rate (10^3~10^8 K/s) [12]. Titanium [13], nickel [14] and aluminum [15] manufactured by SLM method also achieve significant increase of strength, but elongation is much lower than for traditional materials. In order to improve the ductility and reduce residual stress of SLM material, many researchers have investigated process parameter modification and heat treatment. Compared with modification of process parameters, such as layer thickness, scanning speed, laser spot size [16] and volumetric energy density [17], the post heat treatment method is more efficient and more convenient.

Although heat treatment can completely eliminate residual stress in SLM parts [18], it also

directly changes the microstructure. Kong et al. [8] found that dislocations in the sub-grain boundary migrated and disappeared after solution heat treatment. The strength decreased after heat treatment due to a decrease in dislocation density, and better ductility (elongation increased from 40% to 50%) was achieved after full annealing. Yin et al [6] studied the thermal stability and microstructure evolution of SLM 316L from 500 to 800 ℃. At 500℃ and 600 ℃, the sub-grain dislocation cellular structure was stable for up to 400 h. The heat treatment at 700 ℃ for 100 h resulted in coarsening of the cellular structure, and short exposure at 800 ℃ leads to annihilation of the cellular structure. Chao et al. [19] found that inclusions coarsened with temperature increase from 400 ℃ to 1100 ℃. Heat treatment at 800 ℃ for 2 h led to precipitation of embrittling σ phase. The later research mainly focused on evolution of microstructure, such as cellular sub-structure, low angle grain boundaries (LAGBs), nano-oxides and so on, and have not quantitatively analyzed strength variation due to microstructure evolution. Cui [20] and Chen et al. [21] researched strengthening mechanism of the cellular substructure, dislocation density. Hong et al. [11] proposed a combined strengthening mechanism due to LAGBs, density of dislocations and cellular sub-structures. However, this is not sufficiently accurate to predict yield strength in SLM 316L. Up to now, although the influence of heat treatment on microstructure has been investigated, the quantitative relationship between heat treatment, microstructure and tensile properties has not been established. It is difficult to predict yield stress of SLM 316L based on the microstructural characteristics after different heat treatments.

In this study, the influence of heat treatment on tensile properties and microstructure of SLM 316L is investigated systematically. First, SLM 316L, which is fabricated with standard commercial parameters, is heat treated from 550 ℃ to 1150 ℃. Second, tensile tests for different orientations are conducted at room temperature to study the influence of heat treatment on tensile properties. Third, microstructural evolution such as cellular sub-structure, nano-oxide particles and grain size, are revealed and analyzed quantitatively by various methods. Finally, the strengthening contributions of different microstructural factors (e.g. cellular sub-structure, nano-oxide particle and grain boundaries) are coupled with microstructure evolution. The quantitative relationship for heat treatment-microstructure-property is established and is shown to accurately to predict the yield stress of SLM 316L.

2. Experimental details

2.1 Sample preparation

The investigated SLM 316L material is fabricated by SLM 125HL metal printer (SLM solutions, Germany) equipped with a 400W fiber laser. The gas-atomized powder size is distributed from 10 to 45 μm, and its nominal chemical composition (in wt.%) is shown in Table 1. Commercial standard process parameters are used: laser power P = 200 W, scanning speed V = 800 mm/s, layer thickness t = 30 μm, hatch distance H = 120 μm, pre-heat temperature (T_{pr}) = 100 ℃. The fabricating process is under 99.999% argon atmosphere with an argon flow rate of 4 m/s. Based on these parameters, the horizontal blocks and vertical columns for test specimens are fabricated as shown in Fig. 1(a). After manufacturing, the relative density of the SLM 316L is measured by the Archimedes method and is found to be higher than 99.3%, which meets the ASTM F3184-16 standard [22]. The nominal chemical compositions is also shown in Table 1.

The SLM 316L is heat treated in a muffle furnace in air for different conditions: 550 ℃ for 2 h, 550 ℃ for 6 h, 550 ℃ for 325 h, 650 ℃ for 2 h, 750 ℃ for 2 h, 950 ℃ for 2 h, 1095 ℃ for 2 h, 1150 ℃ for 2 h, and cooled in air immediately. The SLM 316L tensile specimens are subsequently machined from the blocks and columns shown in Fig. 1(a). Fig. 1(b) illustrates the geometry of the tensile specimens.

Table 1 Chemical compositions of materials (wt.%)

	Fe	Cr	Ni	Mo	Mn	Si	P	S	C	N
316L powder	Balance	16~18	10~14	2~3	2.00	1.00	0.045	0.03	0.03	0.100
SLM 316L	Balance	18.46	12.49	2.4	0.74	0.75	0.025	0.012	0.040	0.054

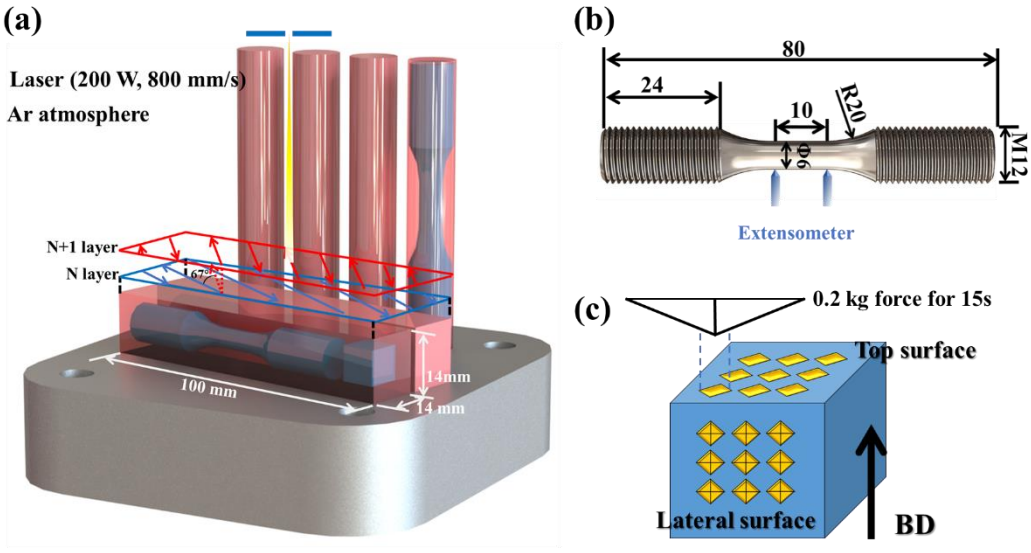

Fig. 1 (a) Schematic of scanning strategy and specimen orientations and positions; (b) geometry of tensile specimens; (c) schematic of micro-hardness test.

2.2 Microstructural characterization

To observe the microstructure and fracture surfaces of SLM 316L, optical microscopy (OM) and scanning electron microscopy (SEM) are used. Specimens for optical microscopy (OM) are metallographically prepared to a 3.5 μm diamond polishing, followed by electrolytic etching using saturated oxalic acid, applying 0.09 A/cm^2 for 45 s at room temperature. Scanning electron microscopy (SEM) characterization is conducted at 15 kV using a TESCAN MIRA field emission gun microscope equipped with an electron backscatter diffraction (EBSD) detector. The diameter of the cellular sub-structure is measured from at least 5 OM images, using image analysis software Image J®. The diameter and number of nano-oxide particles are measured from the SEM fractographies.

EBSD is used to reveal the grain morphologies and misorientation angles. Before EBSD data collection, the analyzed areas are electropolished to remove the deformed layer. The EBSD data is collected using a 0.5 μm step size and post-processed using Channel 5 software.

X-Ray diffraction (XRD) is applied to analyze evolution of phase and total dislocation density. After electropolishing for 40 minutes, phase identification is performed by XRD using a Rigaku Smartlab diffractometer with copper K_α radiation in the 2θ range of 30° to 90°. The rotating rate is 2° per minute.

2.3 Mechanical property measurement

Room-temperature uniaxial tensile tests are conducted at a strain rate of 1.0×10^{-3} s^{-1}, using SINOTEST EQUIPMENT RPL-100 machine equipped with a 100kN load cell. The specimen design with 10 mm gauge length shown in Fig. 1(b) is used in the tensile tests. All experimental data (stress, strain, time, etc.) are collected by EDC220 controller according to the specified time interval. At least two tensile specimens are prepared for each condition. Microhardness is measured on the top and lateral surfaces using a HVS-1000Z microhardness tester with an applied 0.2 kg force and 15 s duration time. Ten indentations are tested on each sample with the average hardness and deviation reported.

3. Results

3.1 Microstructure of as-built SLM 316

As shown in Fig. 2, the microstructural features of the as-built SLM 316 from mm-scale to nm-scale are characterized. Figs. 2(a1) and (a2) show the representative hierarchical microstructure of the lateral and top surfaces in SLM 316L of the mm-scale. The thickness of layer measured from the microstructure is about 30 μm, consistent with powder layer thickness. The track-by-track melting method leads to finger-shaped melting pools, which are surrounded by melt pool boundaries (Red lines in Fig. (a1) and (d)). From the top surface, Fig. 2(b) shows long melt pools which are parallel to each other in the same layer. In next layer, the direction of the melt pool rotates by 67°. Figs. 2(b) and (c) show the grain orientations of the lateral and top surfaces, respectively. The grains observed from the lateral surface are columnar with long studied axis almost parallel to the build direction (BD). From the top surface, the grains exhibit an equiaxed morphology. It is interesting to note that no obvious melt pool boundary is found in the EBSD maps. This indicates that the growth of grains can cross the melt pool boundaries.

At the μm-scale, sub-structures of different shapes are widely distributed in the grains, which are net-shaped structures shown in Fig. 2(d). The diameter (or spacing) of sub-structure is about 1 μm. The sub-structure is not be observed in the EBSD maps, proving that the cellular substructure has same crystallographic orientation. At the nm-scale, Fig. 2(e) shows that the sub-structure has two shapes: columnar and cellular. In addition, many nano-scale particles are adhered to the surfaces of columnar and cellular sub-structures. To identify the chemical elements of the nano-scale particles, energy dispersive spectroscopy (EDS) analysis is conducted. Fig. 2(f) shows that the nano-scale particles have high content of Si and O.

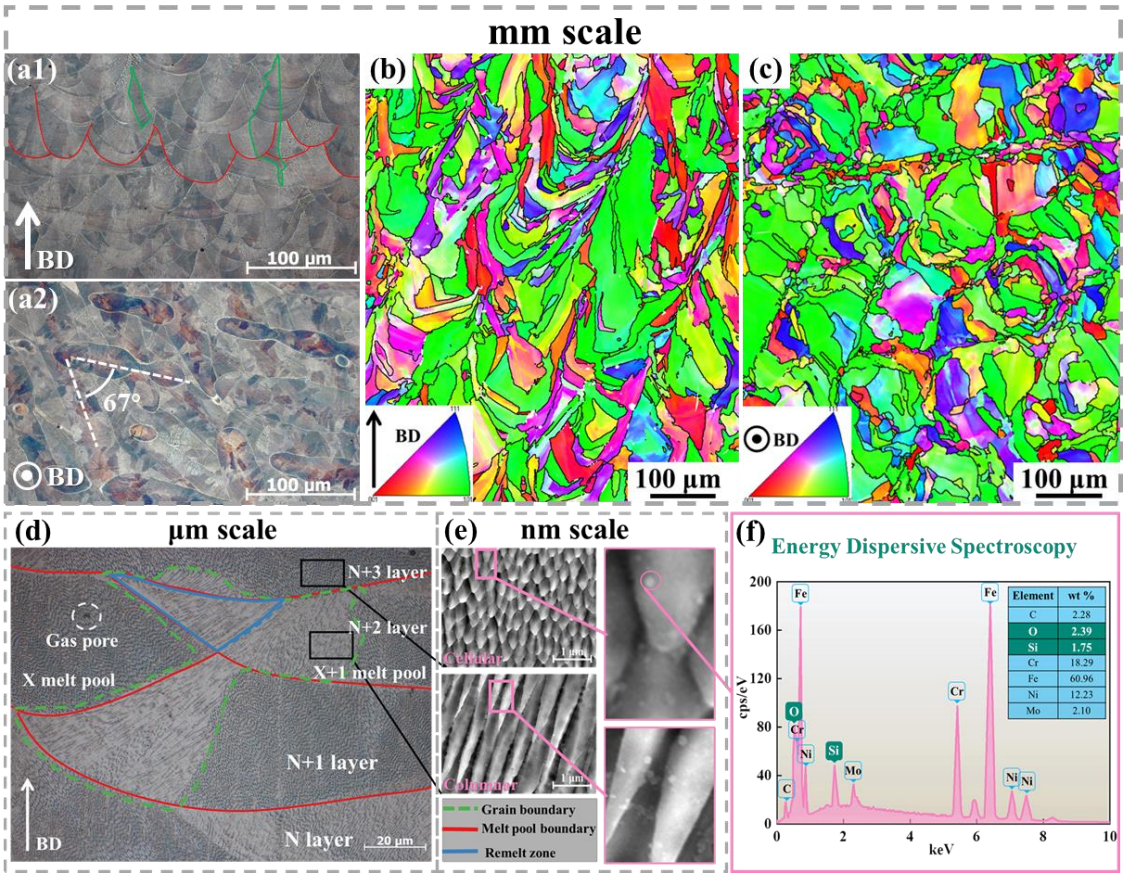

Fig. 2 The characteristic of melting pools on (a1) lateral surface and (a2) top surface; the EBSD inverse pole figure (IPF) orientation maps of (b) lateral surface and (c) top surface; (d) the characteristic of melting pools, grains and sub-structure; (e) greater magnification of cellular and columnar sub-structure and adherent particles; (f) energy dispersive spectroscopy profile of adherent particles.

As observed in Fig. 2(e), the cellular and columnar features seem to be part of the same sub-structure. To confirm this, the microstructures of the lateral and top surfaces at the same location are illustrated by optical microscopy (OM). As shown in Fig. 3, the columnar structure in the lateral surface exhibits a cellular shape in the top surface, indicating that the cellular and columnar sub-structures are the same structure. To avoid confusion of names, the columnar and cellular sub-structures are both referred to hereafter as “cellular sub-structure”. In addition, the EDS analysis is performed across the melt pool boundary. Fig. 3(b) shows that no difference of main elements (i.e. Fe, Cr, Ni, Si) is observed between the melt pool boundary and the matrix.

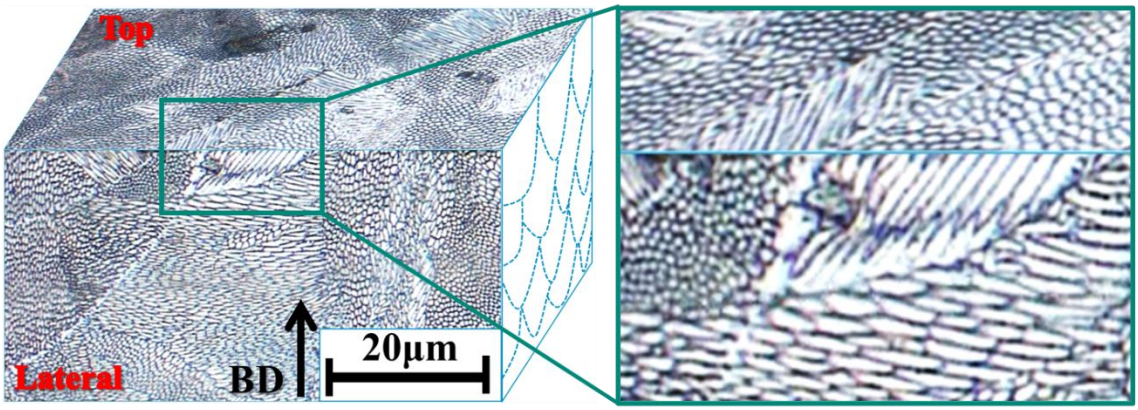

Fig.3 (a)The characteristic of sub-structure from different direction; (b) The element analysis across melting pool boundary.

3.2 Microstructural transformation after heat treatment

Fig. 4 illustrates the XRD patterns of the SLM 316L after heat treatments at different temperatures. The as-built SLM 316L consists purely of austenite (γ) phase, and no new phase is found even though the temperature ranges from 550 ℃ to 1150 ℃, which indicates that SLM 316L has good thermal stability over a 2 h holding time.

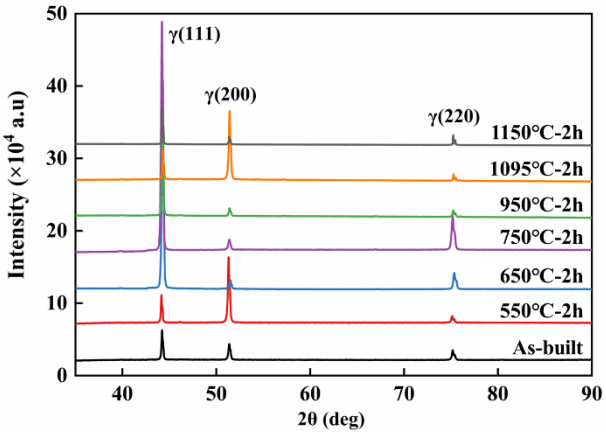

Fig. 4 XRD patterns of SLM 316L under different heat treatment conditions.

Through OM and EBSD analysis, Fig. 5 shows the microstructural transformation after heat treatment, ranging from as-built to distinguishable 1150 ℃. As shown in Fig. 5(a1) and (b1), the cellular sub-structure is still stable and clearly demarcated, and the grain boundaries and melt pool boundaries are clearly visible after 550 ℃ and 650 ℃ heat treatment. Additionally, Fig. 5(a2) and (b2) indicate that grain morphology is still similar to as-built SLM 316L. After 750 ℃ heat treatment, coarsening and annihilation of the cellular sub-structure is observed in Fig. 5(c1), and the melt pool

boundaries become less clearly distinguishable. Fig. 5(c2) shows small coarsening of grains in the EBSD map. After 950 ℃ heat treatment, the cellular sub-structure and melt pool boundaries totally disappear; however, the irregular grains still exist in the matrix. A large number of dark particles are distributed along the grain boundaries. Fig. 5(d1) indicates further grain coarsening and the fine grains disappear gradually due to limited recrystallization. After 1095 ℃ heat treatment, Fig. 5(e1) shows more particles diffused uniformly in the grains, and twin boundaries (red dotted lines) can be observed in some equiaxed austenitic grains. As shown in Fig. 5(e2), further recrystallization occurs in SLM 316L. After 1150 ℃ heat treatment in Fig. 5(f1), the dark particles become even more obvious. EBSD map shows most grains are equiaxed, and many twin boundaries occur in the grains. SLM 316L was recrystallized completely.

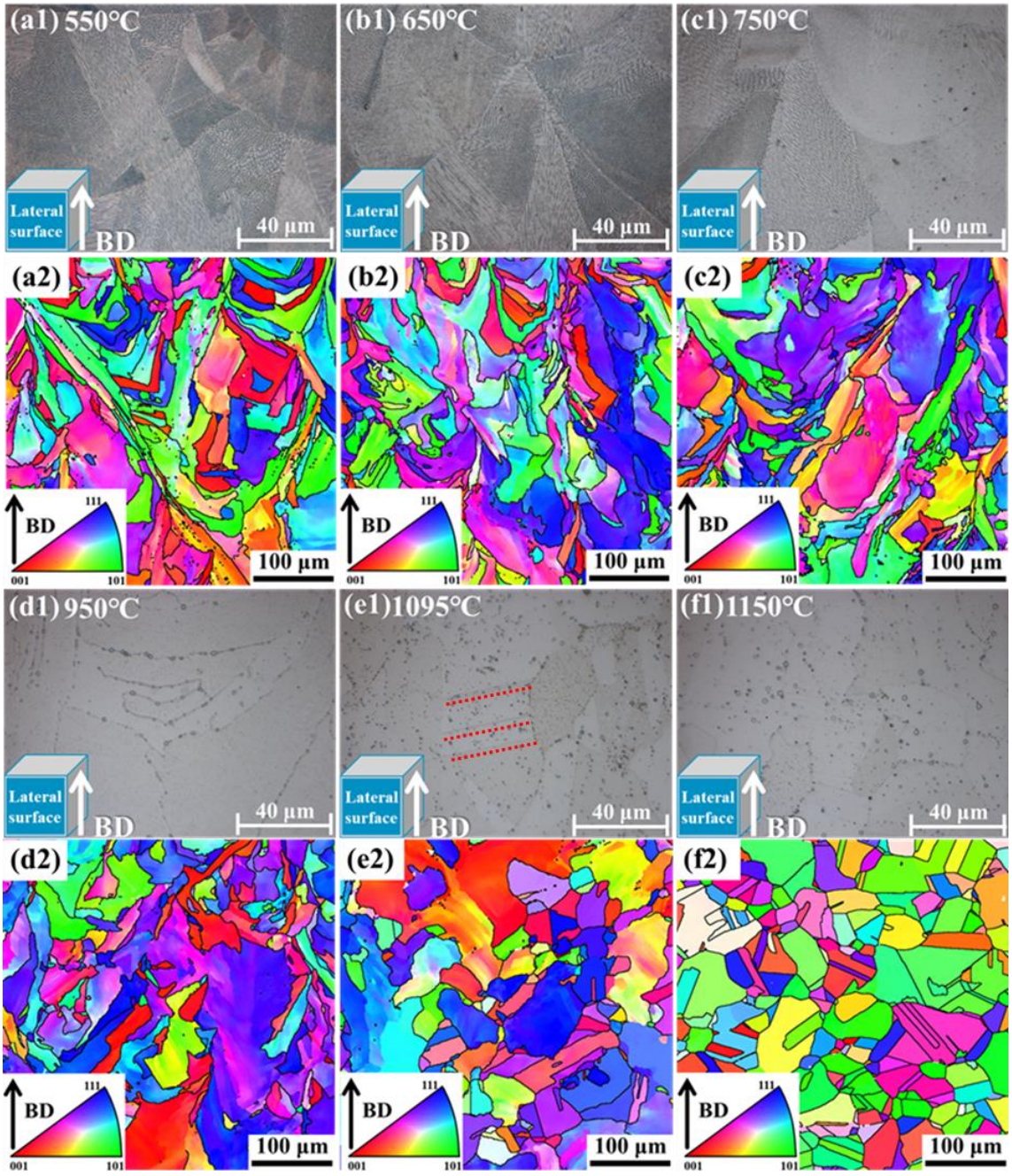

Fig. 5 OM images and IPF orientation maps of lateral surface after different heat-treatment temperatures: (a) 550 ℃; (b) 650 ℃; (c) 750 ℃; (d) 950 ℃; (e) 1095 ℃ and (f) 1150 ℃.

To identify the observed particles in Fig. 5(f2), dimension measurements and chemical composition are carried out. Fig. 6(a) shows the particles distributed in the matrix after 1150 ℃ heat treatment; the average diameter of these particles is about 400 nm. As shown in Fig. 6(b) and (c), the particles have higher O and Si contents than the matrix material, and the EDS analysis result shown in Fig. 6(d) indicates that the particles are similar to the nano-scale particles in Fig. 2(e). According to published results [3, 23], SLM 316L contains nano-oxide particles with similar chemical

composition and morphology to the observed results in Fig. 2(e) and (f) and Fig. 6. Therefore, these particles are identified here as nano-oxide particles.

The SEM-EDS maps demonstrate the high Si and O content in the particles. With respect to chemical composition and morphology, the particles distributed in the grains and along the grain boundaries are the same as the nano-scale particles adhered to the cellular substructure (mentioned in Section 3.1). According to previous research [6, 23], these particles are also then identified as nano-oxide particles.

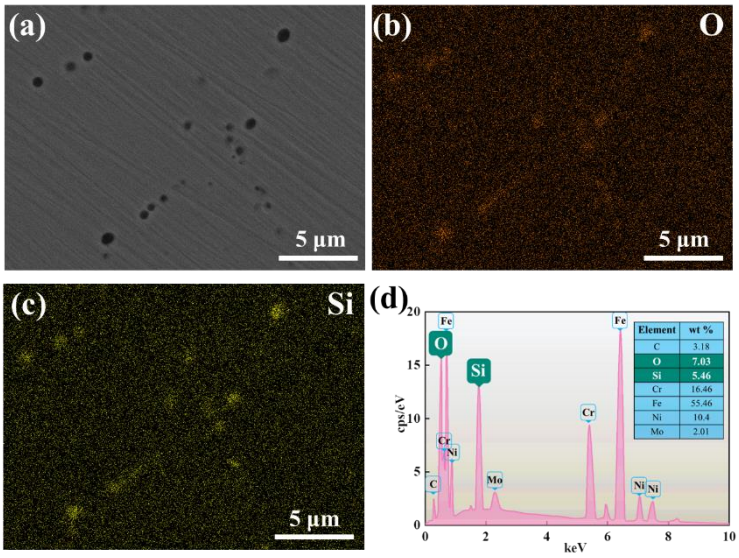

Fig. 6 The SEM-EDS maps of the same area taken for O and Si.

3.3 Variation of mechanical properties

Fig. 7 shows the tensile engineering stress strain curves of the horizontal and vertical oriented specimens for different heat treatment conditions. For the horizontal oriented specimens, the as-built SLM 316L exhibits a quite narrow region of work hardening between the yield strength (YS) of 548.35 MPa and the ultimate tensile strength (UTS) of 671.54 MPa. With increasing heat treatment temperature, both YS and UTS decrease, but elongation increases significantly. After 1150 ℃ heat treatment, SLM 316L exhibits widest region of work hardening and reaches nearly 80% fracture strain, which is almost as high as traditional 316L material [2]. For the vertical specimens, as-built SLM 316L exhibits a typical plastic deformation mode. Work hardening starts to recover gradually with increasing heat treatment temperature. However, no evident necking is observed in the vertical oriented specimens except for the 1150 ℃ heat treatment case, in contrast to horizontal specimens.

This behavior is mainly attributed to the texture along the vertical direction [24, 25].

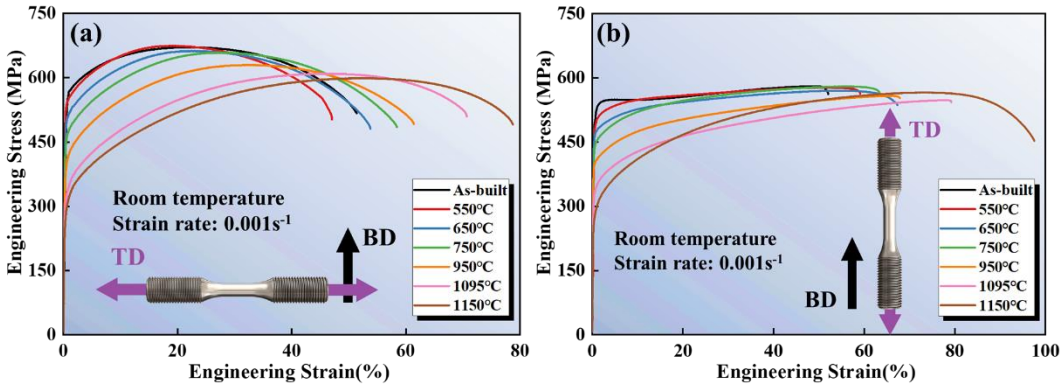

Fig. 7 Engineering stress-engineering strain curves of (a) horizontal oriented specimen, (b) vertical oriented specimen in different heat treatment conditions.

To analyze the variation of YS, UTS and elongation with respect to heat treatment temperature. Fig. 8(a) shows that YS and UTS decrease with heat-treatment temperature in the horizontal oriented specimens, while elongation increases. The reduction in YS is more severe than that of UTS. For the vertical oriented specimens, the variations of YS, UTS and elongation are similar, as shown in Fig. 8(b). YS and UTS in the vertical specimens are lower than in the horizontal specimens. The difference between vertical and horizontal decreases with increasing heat treatment temperature, becoming almost the same at 1150 °C. Variation in effect of heat treatment on YS due to orientation can be divided into two stages. In the first stage, where tensile properties are insensitive to heat treatment temperature, YS decreases gradually up to 750 °C (green dotted line). In the second stage, significant degradation of YS can be observed from 950 °C to 1150 °C (orange dotted line). So, selection of heat treatment temperature in this range should be cautious.

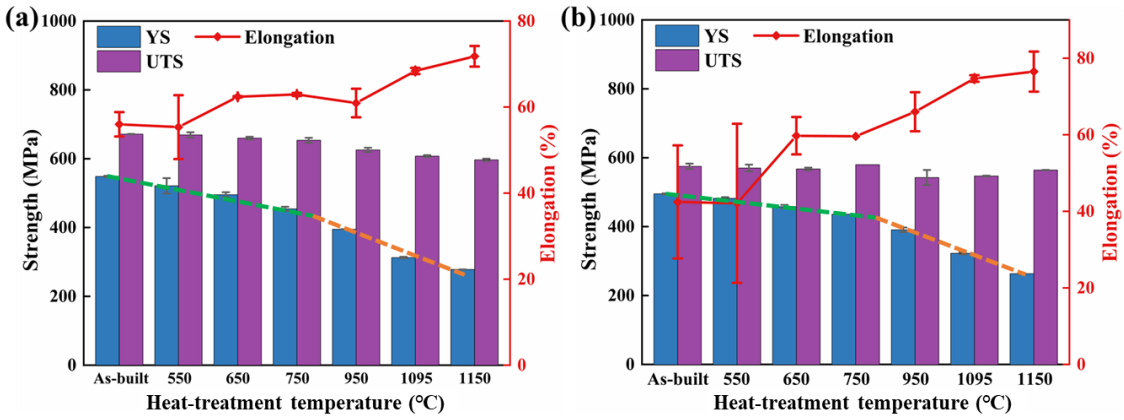

Fig. 8 Influence of heat-treatment temperature on YS, UTS and Elongation of (a) horizontal oriented and (b) vertical oriented specimen.

Figs. 9 (a) and (b) show the microhardness results on the lateral and top surfaces, respectively. Microhardness decreases gradually with increasing temperature, and similar to effect on YS in Fig. 7. Furthermore, the microhardness value on the lateral and top surface are similar in value.

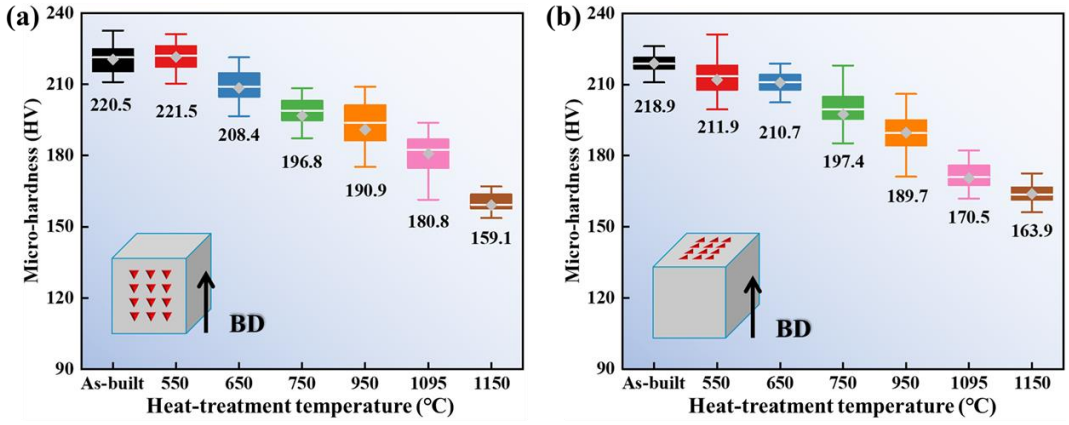

Fig.9 Micro-hardness of (a) lateral and (b) top surface of SLM 316L after different heat treatments.

3.4 Fractographic observation

Figs. 10(a) and (b) show fractography of the horizontal and vertical SLM 316L specimens. Both exhibit typical ductile fracture mode as evidenced by the preponderance of dimples. The dimple size increases significantly with heat treatment temperature. To quantify the evolution of dimple size versus heat treatment temperature, the fractographies of horizontal specimens are statistically measured by image processing software. Fig. 10 (f) indicates that variation of dimple size within conditions from as-built to 750℃ is not significant, similar with result of elongation in Section. 3.3. The observed relation between dimple size and elongation is consistent with our previous published results [26, 27].

Detailed observation of Figs. 10(a) and (b) reveals apparently randomly-distributed particles on the bottom of the dimples. These small particles show obvious coarsening when heat treated of 1150℃. EDS analysis indicates that these particles are rich in Si and O, and then can be identified as nano-oxides. Detailed analysis of these nano-oxide particles is included in Section 4.4.

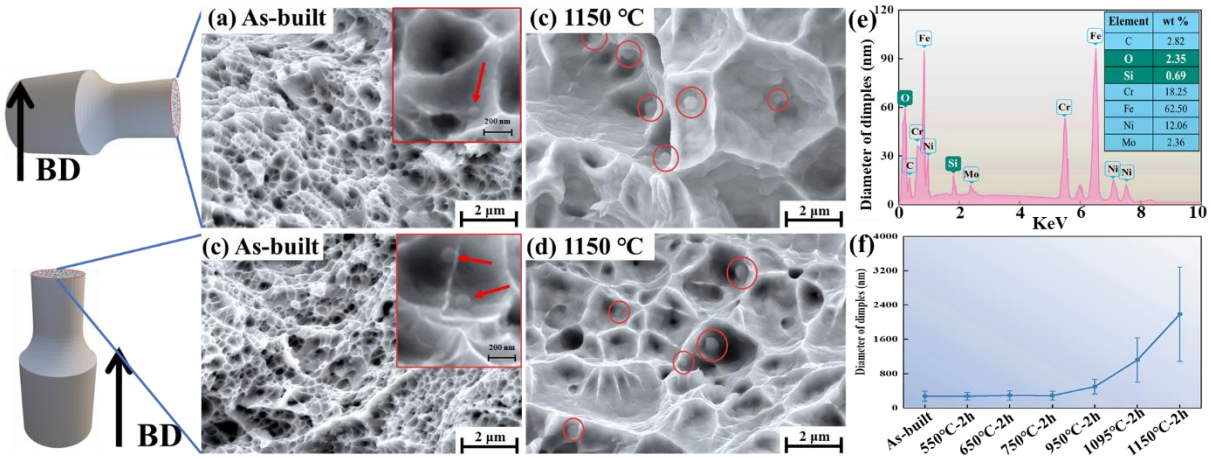

Fig.10 The fractography of as-built and 1150 ℃ heat treated SLM 316L for horizontal and vertical tensile tests ((a) to (d)); (e) EDS spectra result of particles; (f)the evolution of dimple size.

4. Discussion

4.1 Work hardening behavior.

Fig. 11 provides the evolution of normalized work hardening rate (θ) as a function of true stress for different heat-treatment conditions with θ given by:

$$\theta=\frac{1}{\sigma}\left(\frac{d\sigma}{d\varepsilon}\right) \tag{1}$$

where σ, ε are flow stress and true strain, respectively. When θ = 1, i.e. gray dotted line in Fig. 11, the specimen starts necking [3]. In Fig. 11(a), the steady and slowly decreasing hardening rates for 950 ℃, 1095 ℃ and 1150 ℃ heat treatments reflect long periods of work hardening, giving excellent elongation. The sharper decreases of hardening rate for 550 ℃, 650 ℃ and 750 ℃ heat treatments at high stress levels lead to high strength but low elongation. The stable cellular sub-structure for 550 ℃, 650 ℃ and 750 ℃ heat treatments has a pre-existing high density of dislocations and tends to annihilation rather than nucleation. Because work hardening is directly related to dislocation nucleation, the decrease of hardening rate in these heat-treatment conditions is sharper. Fig. 11(b) shows a more rapid decrease in work hardening rate for the vertical tensile tests compared to the horizontal cases, consistent with no obvious work hardening behavior in the stress-strain curves (see Fig. 9(b)). Consistent with no obvious necking in the stress-strain curves (apart from 1150 ℃), the normalized work hardening rate-true stress curves has no distinct intersection with the gray dotted (θ = 1) line. The horizontal and vertical specimen curves are almost the same for 1150 ℃ heat treatment due to similar engineering stress-engineering strain curves, i.e. the work hardening

anisotropy is removed by the 1150 ℃ heat treatment.

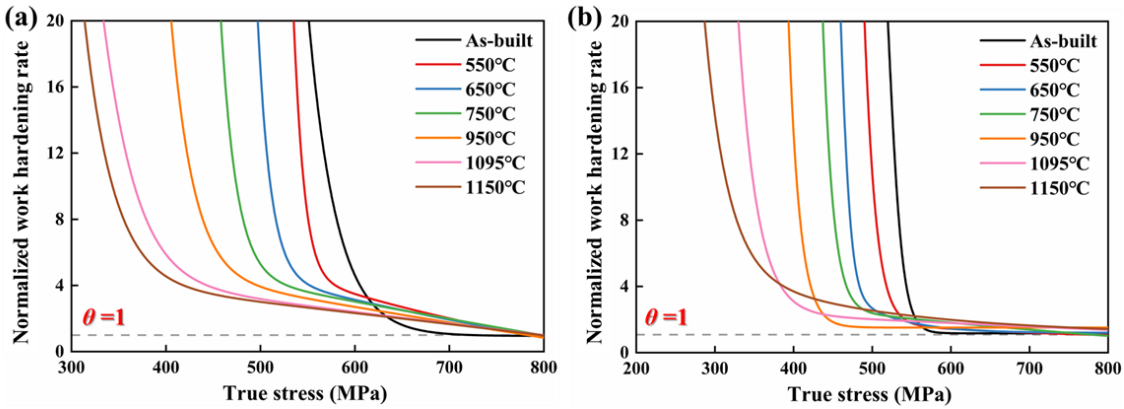

Fig. 11 The work hardening behavior after different heat-treatment conditions for (a) horizontal and (b) vertical tensile tests.

4.2 Total dislocation density.

Based on the profile of XRD curves, the modified Williamson-Hall method (ref) is employed here to determine the dislocation density. The value of the full width at half maximum (FWHM) obtained from peak fitting is substituted into the following modified Williamson-Hall equation [28]:

$$\Delta K = \frac{0.9}{D} + \sqrt{\frac{\pi M^2 b^2}{2}} \rho^{1/2} K \bar{C}^{1/2} + O(K^2 \bar{C}) \tag{2}$$

where $K = 2\sin\theta / \lambda$ and $\Delta K = 2\cos\theta(\Delta\theta) / \lambda$ represent the diffraction angle and the integral breadth of the diffraction peak. Here θ, $\Delta\theta$ and λ are the diffraction angle, full width at half maximum (FWHM) and wavelength of X-rays, respectively. O denotes the higher-order terms in $K\bar{C}^{1/2}$. λ is 0.15405 nm in Cu radiation. D, ρ and b are the average grain size, total dislocation density and magnitude of the Burgers vector (0.255 nm) [28, 29], respectively. M is a constant, identified as 1, based on previous research [30, 31]. $\bar{C}$ is the average contrast factor of dislocations for a particular reflection, defined as

$$\bar{C} = \mathrm{C}_{h00}\left[1 - q\left(\frac{h^2k^2 + h^2l^2 + k^2l^2}{(h^2 + k^2 + l^2)^2}\right)\right] \tag{3}$$

where C_{h00} represents the average contrast factor of *h00* reflection. The value of $\bar{C}$ is determined to

be 0.100, 0.287, 0.147 for $\{111\}$, $\{200\}$, $\{220\}$ reflections, respectively [32]. Based on the slope m of the fitted curve from a ΔK vs. $KC^{1/2}$ plot, the dislocation density can be estimated by the following equation:

$$\rho = 2\frac{m^2}{\pi M^2 b^2} \tag{4}$$

As shown in Fig. 12, the total dislocation density generally decreases with increasing temperature of heat treatment. With annihilation of the cellular sub-structure and grain boundaries, the density of corresponding dislocation decreases gradually after heat treatment.

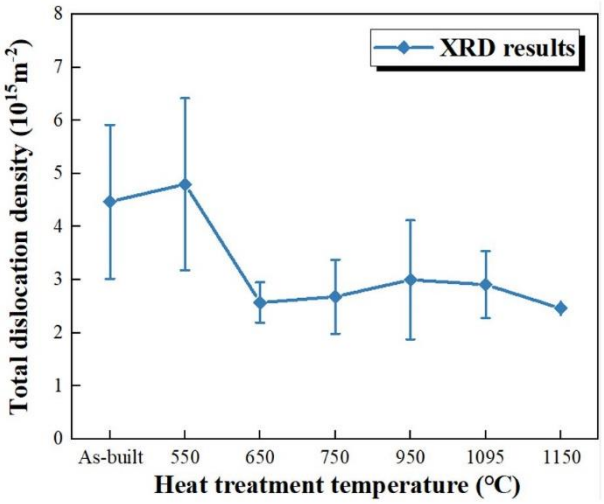

Fig. 12 The evolution of total dislocation density after different temperature heat treatments.

4.3 Strengthening factors.

Apart from the high density of dislocations, a large fraction of low angle grain boundaries (LAGBs) [33], fine grains [21], cellular sub-structure [34] and nano-oxide particles [20] contribute to the high strength of SLM 316L. Commonly, dislocations are not uniformly distributed in the matrix material, but tend to be concentrated near grain boundaries (low angle and high angle grain boundaries) and cellular boundaries [35].

To analyze the evolution of grain boundaries in SLM 316L, Fig. 13(a) shows the frequency distribution of misorientation for the different heat-treatment conditions. For example, the fractions of LAGBs (misorientation angle between 0 and 10°) are 78.7%, 72.0%, 70.3%, 64.7%, 71.1%, 64.2%, and 12.4% in as-built, 550 ℃, 650 ℃, 750 ℃, 950 ℃, 1095 ℃ and 1150 ℃ heat-treated SLM 316L,

respectively. When the temperature reaches 950 ℃, the cellular sub-structure disappears however fraction of LAGBs has a little recovery. It is likely that annihilation of the cellular sub-structure sharply decreases the total number of misorientations, and the fraction of residual LAGBs increases. When the temperature reaches 1095 ℃, the appearance of annealing twin boundaries (Σ3 at 60°) can be observed, in accordance with microstructural images. At 1150 ℃, there is a sharp decrease of LAGBs and obvious increase of Σ3 twin boundaries. The appearance of Σ3 twin boundaries promote further increase of elongation, as shown in Figs. 8 (a) and (b). The misorientation analysis then indicates that a portion of grain boundaries is sensitive to heat treatment temperature.

Hence, the evolution of grain boundaries will lead to variation of grain boundary strengthening. Grain boundary strengthening is based on the classic Hall-Petch relationship, which considers grain boundaries as a barrier for dislocation glide. To avoid possible non-physical effects of singularities due to grain shape and to consider the influence of lower angle grain boundaries on strength, a misorientation angle of 2° is defined as a critical angle of grain boundaries [21]. Fig. 13(b) shows equivalent diameter of grains after different heat-treatment conditions. With increasing temperature, the diameter of grains generally increases. At 1150 ℃, the size increases sharply due to full recrystallization according to the OM results in Fig. 5.

As the most important strengthening factor [11], the cellular sub-structures has same orientation within grain boundaries [36] and can't be considered in grain boundary strengthening. The equivalent diameter of the cellular sub-structure is also influenced by heat-treatment condition. Before annihilation at 950 ℃, it decreases in size with temperature, as shown in Fig. 13(c). In addition, the cellular sub-structure exhibits excellent thermal stability at 550 ℃. After 325h aging at 550 ℃, no obvious coarsening is observed, consisted with Yin's research [6]. This excellent thermal stability of the cellular sub-structure provided high strength for SLM 316L at 550 ℃, which is almost the practiced temperature limit adopted in engineering design [37].

Nano-oxide particles, which can also contribute to the high strength of SLM 316L [23], are also effected by heat-treatment temperature. During the manufacturing process, initial oxide in the powder can completely dissolve into the melt pool due to the extremely high temperature (about 2862 ℃) [38]. With rapid solidification, contributed to extremely high cooling rate (10^6 K/s), nano-oxide particles precipitate into a fine dispersion [23]. Fig. 13(d) indicates that the nano-oxide particles grow slowly from the as-built condition to heat-treatment at 950 ℃, and grow sharply at 1095 ℃ and

1150 ℃. As shown in Fig. 10, the heat-treatment also increases the spacing of particles. The effect of diameter and spacing as strengthening mechanism is discussed in more details in the next section.

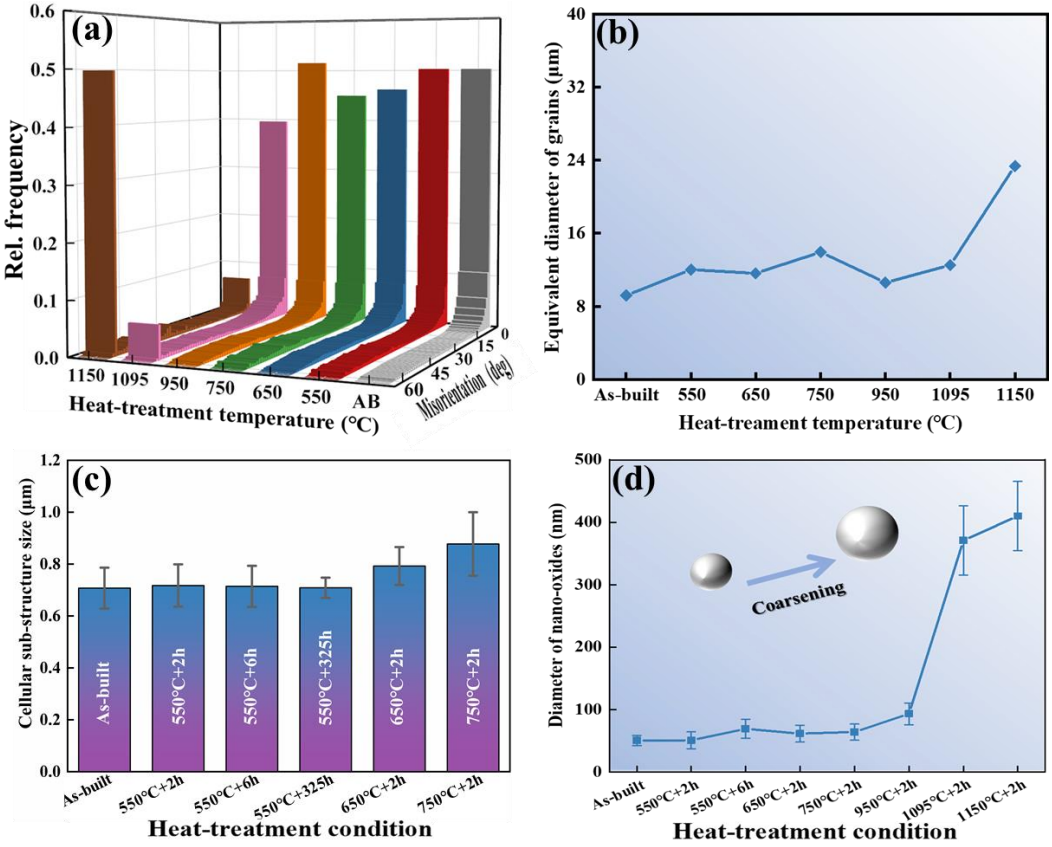

Fig. 13 The influence of heat-treatment on (a) distribution of misorientations; (b) grain size; (c) cellular substructure size and (d) diameter of nano-oxides.

4.4 Yield strength.

Compared with full recrystallization at 1150 ℃, the variations of strengthening factors (e.g., fine grains, cellular sub-structure and nano-oxides) would directly affect the yield strength of SLM 316L after different temperature heat-treatments. As mentioned above, the high density of dislocation is mainly contained in grain boundaries, cellular sub-structure boundaries. The nano-oxides also play an important role of precipitation strengthening[20]. In this section, the grain boundary strengthening, cellular sub-structure strengthening and nano-oxides strengthening from as-built to 1150 ℃ heat-treated condition will be discussed detailly.

Cellular sub-structure strengthening

The cellular sub-structure is a major contributor to strength space [34]. The dense dislocation tangles are concentrated at the cell walls and play a "grain boundary" role in preventing movement of dislocations [39]. In addition, Cr and Mo are also segregated along the walls due to the high cooling rate [34]. The Hall-Petch relationship between yield strength and cell size has been previously reported [11, 34]:

$$\sigma_y = \sigma_0 + K_{cell} \frac{1}{\sqrt{D_{cell}}} \tag{5}$$

where σ_y is yield stress, σ_0 is identified here as 183.31 MPa, K_{cell} is identified as 253.66 MPa·μm$^{0.5}$ and D_{cell} is equivalent average diameter of cellular sub-structure. Based on this relationship, the strengthening contribution from cellular sub-structure can be written as:

$$\Delta\sigma_{cell} = K_{cell} \frac{1}{\sqrt{D_{cell}}} \tag{6}$$

so that a fine cellular sub-structure will increase SLM 316L yield strength. The strengthening contribution due to the cellular sub-structure in as-built SLM 316L here is then about 176.59 MPa. After heat treatment, this value reduces to 174.13 MPa, 157.64 MPa and 142.20 MPa due to coarsening of the sub-structure at 550 ℃, 650 ℃ and 750 ℃, respectively. When the temperature reaches 950 ℃, the cellular sub-structure is annihilated and its strengthening contribution disappears. This decrease of strengthening contribution due to coarsening and annihilation of the cellular substructure lead directly to reduction of YS in SLM 316L.

Nano-oxide particles strengthening

The nano-oxide particles are mainly identified as SiO_2 precipitates [21, 33, 40]. The size and distribution density are closely connected with content of oxygen which is from the atmosphere and initial oxygen in the powder. The diameter and spacing of nano-oxide particles are directly measured from fractography, considering the reduction of fracture area. The average diameter and spacing are 410 nm and 3446.21 nm measured from 1150 ℃ heat-treated specimens. This is consistent with results from metallography, proving the reliability of the fractographic method. Through the latter method, the average spacings of nano-oxide particles are 1008.29 nm, 989.28 nm, 1315.61nm, 1390.04 nm, 1040.92 nm, 2082.79 nm and 3446.21nm after heat-treatments at the different temperatures, respectively. Nano-oxide particles play a role in precipitate strengthening given by Orowan's law [41]:

$$\sigma_{OP} = \frac{\mu \times b}{\lambda - D} \tag{7}$$

where μ is shear modulus (80 GPa), b is magnitude of Burger's vector (0.255 nm) [33] of ordinary dislocations, λ is average spacing, and D is average diameter of oxide-particles. The contribution of nano-oxide particle strengthening for 1150 ℃ fully-recrystallized SLM 316L is determined to be 20.56 MPa. Be referred to this fully-recrystallized condition, the contribution of nano-oxide particle strengthening can be written as:

$$\Delta\sigma_{OP} = \sigma_{OP} - 20.56 \text{ MPa} \tag{8}$$

As shown in Fig. 14(a), the contribution of nano-oxide particle strengthening $\Delta\sigma_{OP}$ generally decreases with increasing heat-treatment temperature. The strengthening effect is significantly weaker than that if the cellular sub-structure up to 950 ℃.

Grain boundary strengthening

The misorientation angle of the cellular sub-structure is less than 2° [34]; the strengthening contribution for such lower misorientation (< 2°) is incorporated in cellular sub-structure contribution (Eq. (6)). Boundaries with higher misorientation angles (> 2°) can be incorprated as general grain boundaries [21, 42]. Physically, grain boundaries represent barriers to dislocation glide during plastic deformation. Grain boundary strengthening is based on the classical Hall-Petch relationship, which can be written as:

$$\Delta\sigma_{GB} = K_{GB} \frac{1}{\sqrt{D_{GB}}} \tag{9}$$

where $\Delta\sigma_{GB}$ is grain boundary strengthening contribution, K_{GB} is Hall-Petch coefficient for SLM 316L，identified here as 289 MPa·μm$^{0.5}$ [21] and D_{GB} is average equivalent diameter of grains. The grain sizes are determined by EBSD method with 2° critical misorientation angle. As shown in Table .2, the grain size increases with heat-treatment temperature. Thus, the grain boundary strengthening contribution decreases gradually from as-built to 950 ℃, and decreases sharply at 950 ℃ and 1150 ℃. Because the columnar grains are parallel to the BD shown in Fig. 2(b), the grain diameter of the top surface is smaller than that of the lateral surface from as-built to 1095 ℃ heat-treatment conditions. After 1150 ℃ full recrystallization, the grain diameters on the lateral and top surfaces are similar since they are equiaxed. These variations in grain diameter are consistent with the microstructural

evolution mentioned in Section 3.2. As shown in Fig. 14, the contribution of grain boundary strengthening (grey blocks) decreases with heat-treatment temperature and is smaller than that of the cellular sub-structure and nano-oxide particles.

Table 2 Grain sizes and strengthening contributions of lateral and top surfaces after different temperature heat-treatments.

Heat-treatment temperature (°C)		As-built	550	650	750	950	1095	1150
Lateral	Grain diameter (μm)	9.19	12.03	11.61	13.95	10.60	12.51	23.36
	Strengthening contribution (MPa)	95.35	83.32	84.80	77.38	88.75	81.68	59.79
Top	Grain diameter (μm)	9.12	10.58	10.47	9.6	9.47	18.61	22.47
	Strengthening contribution (MPa)	95.70	88.85	89.32	93.27	93.91	66.99	60.96

Finally, the three strengthening mechanisms of cellular sub-structure, nano-oxide particles and grain boundaries can be summarized in the evolution of yield strength induced different heat-treatment conditions. Assuming fully-recrystallized SLM 316L as the matrix material, these strengthening contributions of oxide can be added to the yield strength of the matrix as follows:

$$YS_H = YS_m + \Delta\sigma_{cell} + \Delta\sigma_{OP} + \Delta\sigma_{GB} \tag{10}$$

where YS_H is the predicted yield strength of horizontal oriented specimen and YS_m is yield strength of horizontal oriented specimen for 1150 °C fully recrystallized SLM 316L.

As shown in Fig. 14, the predicted values are very close to the measured value, verifying the strengthening mechanisms prepared here for interpretation of the process-structure-property effect of the heat treatment procedure investigated.

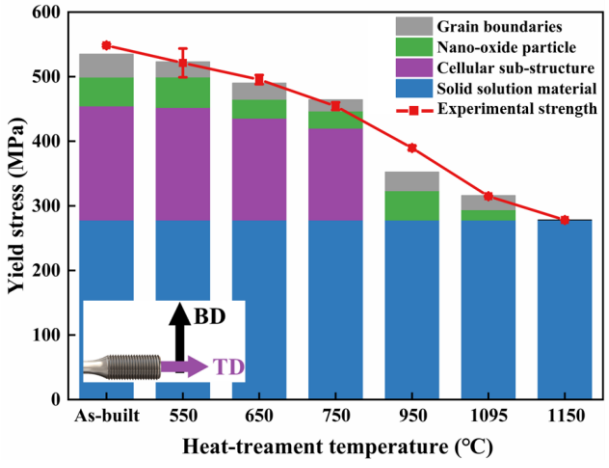

Fig. 14 The effect of heat-treatment temperature on strengthening contribution in SLM 316L of

horizontal orientation (TD: tensile direction).

4.5 The influence of heat-treatment on anisotropy in mechanical properties.

Many SLM materials have anisotropy in mechanical properties, such as steel [25], Ti alloy [13], Ni alloy [43] and Al alloy [44]. Commonly, the yield strength for the horizontal orientation is higher than for the vertical orientation. Firstly, the anisotropy can be attributed to the preferential orientation of columnar grains. During the fabrication process, the temperature gradient is along the BD and promotes the vertical growth of grains. The characterization of columnar grains in the as-built condition can be observed in Fig. 2. The columnar grains lead to larger grain sizes on the lateral surface and smaller grain sizes on the top surface, as shown in Table 2. With increasing heat-treatment temperature, the grain diameters of lateral and top surfaces tend to become equal. The evolution of grain diameter is in accordance with microstructural evolution, as shown in the IPF maps of Fig. 5. After 1150 ℃ heat treatment, the columnar grains are fully recrystallized and transformed into equiaxed grains. Apart from the grains, the melt boundaries annihilate gradually with increasing temperature. Hence, the heat treatment gradually reduces and eliminates anisotropy due to microstructure morphology.

Secondly, internal defects in SLM parts can also lead to anisotropy in mechanical properties. Internal defects are typically classified into three types: porosity, lack-of-fusion defects, and cracks [45], with porosity and lack-of-fusion being common in SLM 316L [46]. Compared with porosity, lack-of-fusion defects are more detrimental to mechanical properties due to the larger volume and sharp edges [47]. Lack-of-fusion defects are commonly dish-like, with a short axis parallel to the BD [45], as show in Fig. 15. Hence the projected area of lack-of-fusion for vertical TD (Fig. 15(b)) is larger than for horizontal TD (Fig. 15(a)), providing a physical explanation for why the degradation of tensile properties under vertical loading is larger than under horizontal loading. The anisotropy of lack-of-fusion defect is another reason for lower yield strength of vertical specimens.

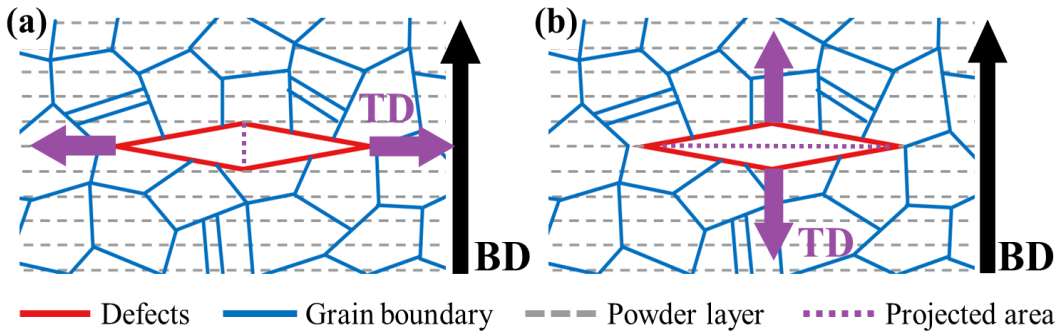

Fig. 15 Different effect of lack-of-fusion on tensile properties of (a) horizontal tensile test; and (b) vertical tensile test.

Typically, lack-of-fusion defects are not be influenced by heat-treatment [48]. Only a thermal-mechanical process such as hot isostatic pressing (HIP) is likely to affect such lack-of-fusion defects, through plastic deformation and pore closure [49]. So, the thermal heat treatment in this study does not affect the lack-of-fusion anisotropy. When anisotropy of microstructure in SLM 316L is eliminated by 1150 ℃ heat treatment, the anisotropy of tensile properties can be attributed solely to lack-of-fusion defects. Most importantly, the same reductions of both YS and UTS of 5.4% for vertical specimen compared to horizontal specimen across after 1150 ℃ heat treatment. This same ratio of reduction in YS and UTS corroborates the conclusion that anisotropic effect of lack-of-fusion defect that on tensile properties is due to the difference in projected area (cf. Fig. 15).

As shown in Fig. 16(a), with the horizontal tensile properties of fully-recrystallized SLM 316L as a datum, cellular sub-structure strengthening, nano-oxide particle strengthening and grain boundary strengthening can be added to this. And, considering the anisotropic effect of lack-of-fusion (5.4% of reduction) is to estimate the vertical yield strength as:

$$YS_V = (1-0.054)\times YS_H = 0.946\times(YS_m + \Delta\sigma_{cell} + \Delta\sigma_{OP} + \Delta\sigma_{GB}) \quad (11)$$

where YS_V and YS_H are predicted yield strengths of vertical and horizontal specimens, respectively and YS_m is yield strength of horizontal specimen after 1150 ℃ heat-treatment. As shown in Fig. 16(b), the strength reduction due to defects is smaller than effect of grain boundary strengthening from as-built to 950 ℃ heat-treatment. After 1095 ℃ heat-treatment, a large number of LAGBs in SLM 316L have been annihilated, and recrystallization begins. Hence, the contribution of grain boundary strengthening is much lower than the strength reduction due to defects. In addition, the predicted YS,

which considers the different strengthening factors and reductions, agree closely with the experimental values.

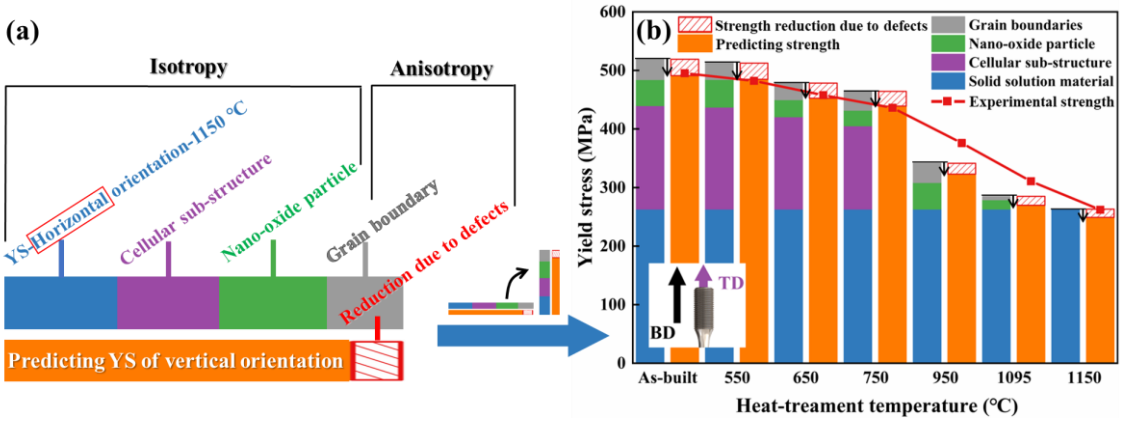

Fig. 16 (a) Schematic of method for predicting YS for vertical orientation; (b) influence of heat-treatment temperature on strengthening contributions for vertical orientation.

5. Conclusions

In this work, the influence of heat treatment on tensile properties and microstructure has been investigated in SLM 316L. Specimens are manufactured using standard commercial parameters that offered a minimum amount of porosity, followed by heat treatments at different temperatures. After heat treatment, mechanical properties and microstructural evolution have been analyzed quantitively. Based on this, the evolutions of different strengthening factors are coupled to predict the yield strength of SLM 316L. Furthermore, anisotropy effects on tensile properties are also discussed. Some conclusions can be drawn from this work:

1. Heat treatment from 550 ℃ to 1150 ℃ obviously decreases YS, UTS and hardness of SLM 316L, whilst increases elongation. The YS, UTS and elongation of horizontal tensile tests are higher than those of vertical tests.
2. SLM 316L consisted of austenite (γ) phase, and heat treatment has no visible effect on this. Heat treatment from 550 ℃ to 750 ℃ causes coarsening of the cellular sub-structure. Heat treatment at 950 ℃ annihilates the cellular sub-structure and melt boundaries. The initial grains are partly recrystallized after heat treatment at 1095 ℃. After 1150 ℃ heat treatment, SLM 316L completes recrystallization.

3. Heat treatment leads to decrease of dislocation density, which is related to coarsening and annihilation of the cellular sub-structure and decrease of LAGBs. In addition, the sizes of grains and nano-oxide particles increases due to heat treatment.
4. The evolution of strengthening factors, e.g. cellular sub-structure, nano-oxide particles and grain boundary, contributes to the change of YS in SLM 316L after heat treatment. A model incorporating the different strengthening mechanisms is shown to provide accurate prediction of YS for SLM 316L.
5. The anisotropy of tensile properties in SLM 316L can be attributed to columnar grains and lack-of-fusion. Anisotropy due to lack-of-fusion defects leads to 5.4% reduction of YS in vertical tensile properties. When anisotropic effects of columnar grains and lack-of-fusion defect are incorporated into the model based on horizontal tensile properties, it is also able to predict the vertical tensile YS for SLM 316L.

Acknowledgement

The authors gratefully acknowledge the financial support of the Key Project of University Natural Science Research in Jiangsu province (20KJA460002), Postgraduate Research & Practice Innovation Program of Jiangsu Province (KYCX21_1119). X. Yang and S. Leen acknowledge the financial support of Science Foundation Ireland as part of I-Form Advanced Manufacturing Research Centre under grant number SFI/16/RC/3872. Chenglu Liu also acknowledge the financial support of General University Science Research Project of Jiangsu Province (20KJB430011).

Reference:

[1]. Tan C, Weng F, Sui S, et al. Progress and perspectives in laser additive manufacturing of key aeroengine materials[J]. International Journal of Machine Tools and Manufacture, 2021, 170: 103804. https://doi.org/10.1016/j.ijmachtools.2021.103804

[2]. Yin Y J, Sun J Q, Guo J, et al. Mechanism of high yield strength and yield ratio of 316 L stainless steel by additive manufacturing[J]. Materials Science and Engineering: A, 2019, 744: 773-777. https://doi.org/10.1016/j.msea.2018.12.092

[3]. Fu J, Qu S, Ding J, et al. Comparison of the microstructure, mechanical properties and distortion of stainless steel 316 L fabricated by micro and conventional laser powder bed fusion[J]. Additive Manufacturing, 2021, 44: 102067. https://doi.org/10.1016/j.addma.2021.102067

[4]. Yap C Y, Chua C K, Dong Z L, et al. Review of selective laser melting: Materials and applications[J]. Applied physics reviews, 2015, 2(4): 041101. https://doi.org/10.1063/1.4935926

[5]. Pham M S, Dovgyy B, Hooper P A, et al. The role of side-branching in microstructure development in laser powder-

bed fusion[J]. Nature communications, 2020, 11(1): 1-12. https://doi.org/10.1038/s41467-020-14453-3
[6]. Yin H, Song M, Deng P, et al. Thermal stability and microstructural evolution of additively manufactured 316L stainless steel by laser powder bed fusion at 500–800°C[J]. Additive Manufacturing, 2021, 41: 101981. https://doi.org/10.1016/j.addma.2021.101981
[7]. Gusarov A V, Kruth J P. Modelling of radiation transfer in metallic powders at laser treatment[J]. International Journal of Heat and Mass Transfer, 2005, 48(16): 3423-3434. https://doi.org/10.1016/j.ijheatmasstransfer.2005.01.044
[8]. Kong D, Dong C, Ni X, et al. Mechanical properties and corrosion behavior of selective laser melted 316L stainless steel after different heat treatment processes[J]. Journal of Materials Science & Technology, 2019, 35(7): 1499-1507. https://doi.org/10.1016/j.jmst.2019.03.003
[9]. Abe F, Osakada K, Shiomi M, et al. The manufacturing of hard tools from metallic powders by selective laser melting[J]. Journal of materials processing technology, 2001, 111(1-3): 210-213. https://doi.org/10.1016/S0924-0136(01)00522-2
[10]. Hong Y, Zhou C, Zheng Y, et al. Formation of strain-induced martensite in selective laser melting austenitic stainless steel[J]. Materials Science and Engineering: A, 2019, 740: 420-426.
https://doi.org/10.1016/j.msea.2018.10.121
[11]. Hong Y, Zhou C, Zheng Y, et al. The cellular boundary with high density of dislocations governed the strengthening mechanism in selective laser melted 316L stainless steel[J]. Materials Science and Engineering: A, 2021, 799: 140279.https://doi.org/10.1016/j.msea.2020.140279
[12]. Vilaro T, Colin C, Bartout J D, et al. Microstructural and mechanical approaches of the selective laser melting process applied to a nickel-base superalloy[J]. Materials Science and Engineering: A, 2012, 534: 446-451.https://doi.org/10.1016/j.msea.2011.11.092
[13]. Simonelli M, Tse Y Y, Tuck C. Effect of the build orientation on the mechanical properties and fracture modes of SLM Ti–6Al–4V[J]. Materials Science and Engineering: A, 2014, 616: 1-11. https://doi.org/10.1016/j.msea.2014.07.086
[14]. Lee J, Lee M, Jung I D, et al. Correlation between microstructure and tensile properties of STS 316L and inconel 718 fabricated by selective laser melting (SLM)[J]. Journal of Nanoscience and Nanotechnology, 2020, 20(11): 6807-6814. https://doi.org/10.1166/jnn.2020.18792
[15]. Prashanth K G, Scudino S, Eckert J. Defining the tensile properties of Al-12Si parts produced by selective laser melting[J]. Acta Materialia, 2017, 126: 25-35. https://doi.org/10.1016/j.actamat.2016.12.044
[16]. Tolosa I, Garciandía F, Zubiri F, et al. Study of mechanical properties of AISI 316 stainless steel processed by "selective laser melting", following different manufacturing strategies[J]. The International Journal of Advanced Manufacturing Technology, 2010, 51(5): 639-647.
https://doi.org/10.1007/s00170-010-2631-5
[17]. Simson T, Emmel A, Dwars A, et al. Residual stress measurements on AISI 316L samples manufactured by selective laser melting[J]. Additive Manufacturing, 2017, 17: 183-189. https://doi.org/10.1016/j.addma.2017.07.007
[19]. Chao Q, Thomas S, Birbilis N, et al. The effect of post-processing heat treatment on the microstructure, residual stress and mechanical properties of selective laser melted 316L stainless steel[J]. Materials Science and Engineering: A, 2021, 821: 141611. https://doi.org/10.1016/j.msea.2021.141611
[20]. Cui L, Jiang S, Xu J, et al. Revealing relationships between microstructure and hardening nature of additively manufactured 316L stainless steel[J]. Materials & Design, 2021, 198: 109385. https://doi.org/10.1016/j.matdes.2020.109385
[21]. Chen S, Ma G, Wu G, et al. Strengthening mechanisms in selective laser melted 316L stainless steel[J]. Materials Science and Engineering: A, 2022, 832: 142434. https://doi.org/10.1016/j.msea.2021.142434
[22]. ASTM International, F3184-16 Standard Specification for Additive Manufacturing Stainless Steel Alloy (UNS S31603) with Powder Bed Fusion, ASTM International, West Conshohocken, PA, 2016.

[23]. Yan F, Xiong W, Faierson E, et al. Characterization of nano-scale oxides in austenitic stainless steel processed by powder bed fusion[J]. Scripta Materialia, 2018, 155: 104-108. https://doi.org/10.1016/j.scriptamat.2018.06.011
[24]. Wang X, Muñiz-Lerma J A, Sanchez-Mata O, et al. Characterization of single crystalline austenitic stainless steel thin struts processed by laser powder bed fusion[J]. Scripta Materialia, 2019, 163: 51-56. https://doi.org/10.1016/j.scriptamat.2018.12.032
[25]. Güden M, Yavaş H, Tanrıkulu A A, et al. Orientation dependent tensile properties of a selective-laser-melt 316L stainless steel[J]. Materials Science and Engineering: A, 2021, 824: 141808. https://doi.org/10.1016/j.msea.2021.141808
[26]. Wang X, Zhang W, Ni J, et al. Quantitative description between pre-fatigue damage and residual tensile properties of P92 steel[J]. Materials Science and Engineering: A, 2019, 744: 415-425. https://doi.org/10.1016/j.msea.2018.12.029
[27]. Zhang W, Zhang T, Wang X, et al. Remaining creep properties and fracture behaviour of P92 steel welded joint under prior low cycle fatigue loading[J]. Journal of Materials Research and Technology, 2020, 9(4): 7887-7899. https://doi.org/10.1016/j.jmrt.2020.05.078
[28]. Sprouster D J, Cunningham W S, Halada G P, et al. Dislocation microstructure and its influence on corrosion behavior in laser additively manufactured 316L stainless steel[J]. Additive Manufacturing, 2021, 47: 102263. https://doi.org/10.1016/j.addma.2021.102263
[29]. Shamsujjoha M, Agnew S R, Fitz-Gerald J M, et al. High strength and ductility of additively manufactured 316L stainless steel explained[J]. Metallurgical and Materials Transactions A, 2018, 49(7): 3011-3027. https://doi.org/10.1007/s11661-018-4607-2
[30]. Ribárik G, Ungár T. Characterization of the microstructure in random and textured polycrystals and single crystals by diffraction line profile analysis[J]. Materials Science and Engineering: A, 2010, 528(1): 112-121. https://doi.org/10.1016/j.msea.2010.08.059
[31]. Starck L F, Zilnyk K D, Senra A L T, et al. In Situ x-ray Diffraction Study of the Deformation of an AISI 316L Stainless Steel Produced by Laser Powder Bed Fusion[J]. Journal of Materials Engineering and Performance, 2022: 1-14. https://doi.org/10.1007/s11665-022-06851-z
[32]. Xu Y, Nie Y, Wang M, et al. The effect of microstructure evolution on the mechanical properties of martensite ferritic steel during long-term aging[J]. Acta Materialia, 2017, 131: 110-122. https://doi.org/10.1016/j.actamat.2017.03.045
[33]. Voisin T, Forien J B, Perron A, et al. New insights on cellular structures strengthening mechanisms and thermal stability of an austenitic stainless steel fabricated by laser powder-bed-fusion[J]. Acta Materialia, 2021, 203: 116476. https://doi.org/10.1016/j.actamat.2020.11.018
[34]. Wang Y M, Voisin T, McKeown J T, et al. Additively manufactured hierarchical stainless steels with high strength and ductility[J]. Nature materials, 2018, 17(1): 63-71. https://doi.org/10.1038/nmat5021
[35]. Li J, Yi M, Wu H, et al. Fine-grain-embedded dislocation-cell structures for high strength and ductility in additively manufactured steels[J]. Materials Science and Engineering: A, 2020, 790: 139736. https://doi.org/10.1016/j.msea.2020.139736
[36]. Bertsch K M, De Bellefon G M, Kuehl B, et al. Origin of dislocation structures in an additively manufactured austenitic stainless steel 316L[J]. Acta Materialia, 2020, 199: 19-33. https://doi.org/10.1016/j.actamat.2020.07.063
[37]. Hong S G, Lee S B. The tensile and low-cycle fatigue behavior of cold worked 316L stainless steel: influence of dynamic strain aging[J]. International Journal of Fatigue, 2004, 26(8): 899-910. https://doi.org/10.1016/j.ijfatigue.2003.12.002
[38]. Tran H C, Lo Y L. Heat transfer simulations of selective laser melting process based on volumetric heat source with powder size consideration[J]. Journal of Materials Processing Technology, 2018, 255: 411-425. https://doi.org/10.1016/j.jmatprotec.2017.12.024
[39]. Riabov D, Leicht A, Ahlström J, et al. Investigation of the strengthening mechanism in 316L stainless steel produced with laser powder bed fusion[J]. Materials Science and Engineering: A, 2021, 822: 141699.

https://doi.org/10.1016/j.msea.2021.141699
[40]. Godec M, Zaefferer S, Podgornik B, et al. Quantitative multiscale correlative microstructure analysis of additive manufacturing of stainless steel 316L processed by selective laser melting[J]. Materials Characterization, 2020, 160: 110074. https://doi.org/10.1016/j.matchar.2019.110074
[41]. Orowan E. Symp. on Internal Stress in Metals and Alloys[J]. The Institute of Metals, London, 1948, 451.
[42]. Kuhlmann-Wilsdorf D, Hansen N. Geometrically necessary, incidental and subgrain boundaries[J]. Scripta metallurgica et materialia, 1991, 25(7): 1557-1562.
https://doi.org/10.1016/0956-716X(91)90451-6
[43]. Du D, Dong A, Shu D, et al. Influence of build orientation on microstructure, mechanical and corrosion behavior of Inconel 718 processed by selective laser melting[J]. Materials Science and Engineering: A, 2019, 760: 469-480. https://doi.org/10.1016/j.msea.2019.05.013
[44]. Menezes J T O, Castrodeza E M, Casati R. Effect of build orientation on fracture and tensile behavior of A357 Al alloy processed by Selective Laser Melting[J]. Materials Science and Engineering: A, 2019, 766: 138392. https://doi.org/10.1016/j.msea.2019.138392
[45]. Bartlett J L, Heim F M, Murty Y V, et al. In situ defect detection in selective laser melting via full-field infrared thermography[J]. Additive Manufacturing, 2018, 24: 595-605. https://doi.org/10.1016/j.addma.2018.10.045
[46]. Stern F, Kleinhorst J, Tenkamp J, et al. Investigation of the anisotropic cyclic damage behavior of selective laser melted AISI 316L stainless steel[J]. Fatigue & Fracture of Engineering Materials & Structures, 2019, 42(11): 2422-2430. https://doi.org/10.1111/ffe.13029
[47]. Yadollahi A, Shamsaei N, Thompson S M, et al. Effects of building orientation and heat treatment on fatigue behavior of selective laser melted 17-4 PH stainless steel[J]. International Journal of Fatigue, 2017, 94: 218-235 .https://doi.org/10.1016/j.ijfatigue.2016.03.014
[48]. Maskery I, Aboulkhair N T, Corfield M R, et al. Quantification and characterisation of porosity in selectively laser melted Al–Si10–Mg using X-ray computed tomography[J]. Materials Characterization, 2016, 111: 193-204. https://doi.org/10.1016/j.matchar.2015.12.001
[49]. Yu C, Huang Z, Zhang Z, et al. Effects of sandblasting and HIP on very high cycle fatigue performance of SLM-fabricated IN718 superalloy[J]. Journal of Materials Research and Technology, 2022, 18: 29-43. https://doi.org/10.1016/j.jmrt.2022.02.077